教育部科技查新工作站（G09）
检索证明

委托单位	武汉理工大学
委托人	李欣媛
检索要求	指定检索委托人送检论文《Gradient Pores Enhance Charge Storage Density of Carbonaceous Cathodes for Zn-Ion Capacitor》被 SCI-E 数据库收录、中科院期刊分区升级版、JCR 期刊分区(最新年 2023)信息
数据库	收录篇数
SCI-E	1 篇（第 1 作者）
中科院期刊分区	期刊分区信息

中国科学院文献情报中心期刊分区表升级版　首页　排名　反馈 ▾　退出

2023年 ▾

ADVANCED MATERIALS

刊名	ADVANCED MATERIALS
年份	2023
ISSN	0935-9648
Review	否
Open Access	否
Web of Science	SCIE

	学科	分区	Top期刊
大类	材料科学	1	是
小类	CHEMISTRY, MULTIDISCIPLINARY 化学：综合	1	
	CHEMISTRY, PHYSICAL 物理化学	1	
	MATERIALS SCIENCE, MULTIDISCIPLINARY 材料科学：综合	1	
	NANOSCIENCE & NANOTECHNOLOGY 纳米科技	1	-
	PHYSICS, APPLIED 物理：应用	1	
	PHYSICS, CONDENSED MATTER 物理：凝聚态物理	1	

JCR

ADVANCED MATERIALS

Publisher name: WILEY-V C H VERLAG GMBH

JCR Category	Category Rank	Category Quartile
CHEMISTRY, MULTIDISCIPLINARY *In SCIE edition*	5/230	Q1
CHEMISTRY, PHYSICAL *In SCIE edition*	4/178	Q1
MATERIALS SCIENCE, MULTIDISCIPLINARY *In SCIE edition*	11/438	Q1
NANOSCIENCE & NANOTECHNOLOGY *In SCIE edition*	4/140	Q1
PHYSICS, APPLIED *In SCIE edition*	6/179	Q1
PHYSICS, CONDENSED MATTER *In SCIE edition*	3/79	Q1

Source: Journal Citation Reports 2023. Learn more

声　明	委托人接受本证明，视为对本证明所列论文检索信息已核对，确认无误，若有不实，由委托人承担全部责任。		
检索人	李欣媛	审核人	

教育部科技查新工作站（G09）

2024 年 6 月 24 日

信息来源：SCI-E☑、JCR☑、中国科学院文献情报中心期刊分区表☑

1 result from Science Citation Index Expanded (SCI-EXPANDED):

Analyze Results | Citation Report | Create Alert

Gradient Pores Enhance Charge Storage Density of Carbonaceous Cathodes for Zn-Ion Capacitor (Title) Search

Add Keywords

Publications You may also like... Copy query link

Refine results

0/1 Add To Marked List Export Sort by: Relevance

Search within results...

1 of 1

Quick Filters

None of the results contain data in this field.

Publication Years

Show Final Publication Year

2024 1

Document Types

Article 1

Researcher Profiles

Show Researcher Profiles

Fan, Hong Jin 1
Zhang, Bao 1
Mai, Liqiang 1
Hu, Ping 1
Cai, Congcong 1

See all >

Web of Science Categories

Citation Topics Meso

Citation Topics Micro

Web of Science Index

Affiliations

1 Gradient Pores Enhance Charge Storage Density of Carbonaceous Cathodes for Zn-Ion Capacitor

Li, XY; Cai, CC; (...); Fan, HJ

Jun 2024 | ADVANCED MATERIALS 36 (23)

Engineering carbonaceous cathode materials with adequately accessible active sites is crucial for unleashing their charge storage potential. Herein, activated meso-micropo ... Show more

Full Text at Publisher •••

3 Citations

66 References

Related records

Page size 50 1 of 1

1 record matched your query of the 42,047,959 in the data limits you selected.

Web of Science™

1 record(s) printed from Clarivate Web of Science

Record 1 of 1

Title: Gradient Pores Enhance Charge Storage Density of Carbonaceous Cathodes for Zn-Ion Capacitor

Author(s): Li, XY (Li, Xinyuan); Cai, CC (Cai, Congcong); Hu, P (Hu, Ping); Zhang, B (Zhang, Bao); Wu, PJ (Wu, Peijie); Fan, H (Fan, Hao); Chen, Z (Chen, Zhuo); Zhou, L (Zhou, Liang); Mai, LQ (Mai, Liqiang); Fan, HJ (Fan, Hong Jin)

Source: ADVANCED MATERIALS **Volume:** 36 **Issue:** 23 **DOI:** 10.1002/adma.202400184 **Early Access Date:** FEB 2024 **Published Date:** 2024 JUN

Times Cited in Web of Science Core Collection: 3

Total Times Cited: 3

Abstract: Engineering carbonaceous cathode materials with adequately accessible active sites is crucial for unleashing their charge storage potential. Herein, activated meso-microporous shell carbon (MMSC-A) nanofibers are constructed to enhance the zinc ion storage density by forming a gradient-pore structure. A dominating pore size of 0.86 nm is tailored to cater for the solvated [Zn(H2O)6]2+. Moreover, these gradient porous nanofibers feature rapid ion/electron dual conduction pathways and offer abundant active surfaces with high affinity to electrolyte. When employed in Zn-ion capacitors (ZICs), the electrode delivers significantly enhanced capacity (257 mAh g-1), energy density (200 Wh kg-1 at 78 W kg-1), and cyclic stability (95% retention after 10 000 cycles) compared to nonactivated carbon nanofibers electrode. A series of in situ characterization techniques unveil that the improved Zn2+ storage capability stems from size compatibility between the pores and [Zn(H2O)6]2+, the co-adsorption of Zn2+, H+, and SO42-, as well as reversible surface chemical interaction. This work presents an effective method to engineering meso-microporous carbon materials toward high energy-density storage, and also offers insights into the Zn2+ storage mechanism in such gradient-pore structures.
The charge density of Zn-ion capacitor (ZIC) is significantly enhanced by deploying an activated meso-microporous shell carbon (MMSC-A) nanofibers. The tailored pore size and gradient-pore structure endow the nanofibers with unusual charge storage mechanism, as elucidated by multiple in situ means. image

Accession Number: WOS:001164379800001

Addresses: [Li, Xinyuan; Cai, Congcong; Hu, Ping; Wu, Peijie; Fan, Hao; Chen, Zhuo; Zhou, Liang; Mai, Liqiang] Wuhan Univ Technol, State Key Lab Adv Technol Mat Synth & Proc, Wuhan 430070, Peoples R China.
[Li, Xinyuan; Zhang, Bao; Fan, Hong Jin] Nanyang Technol Univ, Sch Phys & Math Sci, Singapore 637371, Singapore.
[Zhou, Liang; Mai, Liqiang] Wuhan Univ Technol, Hubei Longzhong Lab, Xiangyang 441000, Hubei, Peoples R China.

Corresponding Address: Zhou, L; Mai, LQ (corresponding author), Wuhan Univ Technol, State Key Lab Adv Technol Mat Synth & Proc, Wuhan 430070, Peoples R China.
Fan, HJ (corresponding author), Nanyang Technol Univ, Sch Phys & Math Sci, Singapore 637371, Singapore.
Zhou, L; Mai, LQ (corresponding author), Wuhan Univ Technol, Hubei Longzhong Lab, Xiangyang 441000, Hubei, Peoples R China.

E-mail Addresses: liangzhou@whut.edu.cn; mlq518@whut.edu.cn; fanhj@ntu.edu.sg

Affiliations: Wuhan University of Technology; Nanyang Technological University; Wuhan University of Technology

ISSN: 0935-9648

eISSN: 1521-4095

Output Date: 2024-06-24

End of File

ADVANCED MATERIALS
www.advmat.de

Gradient Pores Enhance Charge Storage Density of Carbonaceous Cathodes for Zn-Ion Capacitor

Xinyuan Li, Congcong Cai, Ping Hu, Bao Zhang, Peijie Wu, Hao Fan, Zhuo Chen, Liang Zhou, Liqiang Mai,* and Hong Jin Fan**

Engineering carbonaceous cathode materials with adequately accessible active sites is crucial for unleashing their charge storage potential. Herein, activated meso-microporous shell carbon (MMSC-A) nanofibers are constructed to enhance the zinc ion storage density by forming a gradient-pore structure. A dominating pore size of 0.86 nm is tailored to cater for the solvated $[Zn(H_2O)_6]^{2+}$. Moreover, these gradient porous nanofibers feature rapid ion/electron dual conduction pathways and offer abundant active surfaces with high affinity to electrolyte. When employed in Zn-ion capacitors (ZICs), the electrode delivers significantly enhanced capacity (257 mAh g^{-1}), energy density (200 Wh kg^{-1} at 78 W kg^{-1}), and cyclic stability (95% retention after 10 000 cycles) compared to nonactivated carbon nanofibers electrode. A series of in situ characterization techniques unveil that the improved Zn^{2+} storage capability stems from size compatibility between the pores and $[Zn(H_2O)_6]^{2+}$, the co-adsorption of Zn^{2+}, H^+, and SO_4^{2-}, as well as reversible surface chemical interaction. This work presents an effective method to engineering meso-microporous carbon materials toward high energy-density storage, and also offers insights into the Zn^{2+} storage mechanism in such gradient-pore structures.

1. Introduction

The soaring demands for large-scale energy storage and efficient power output have propelled significant advance in electrochemical energy storage (EES) systems.[1] In contrast to metal-ion batteries with sluggish ions dynamics,[2] metal-ion capacitors stand out as a prospective EES device that integrates the high-energy-density battery anode and the high-power-density capacitive cathode.[3] Monovalent ion capacitors (e.g., Li^+, Na^+, K^+) have been extensively investigated; but the concerns of the flammability and toxicity associated with the organic electrolytes have prompted attentions to aqueous systems.[4] Particularly, metallic zinc demonstrates great compatibility in both humid and oxygen environment. Zinc features high theoretical gravimetric specific capacity (823 mAh g^{-1}), low redox potential (−0.76 V vs standard hydrogen electrode), and natural abundance (≈300-fold that of lithium). Compared to the intercalation type anode materials, zinc features the fast deposition/striping redox reaction.[5] These merits make Zn a suitable anode material for aqueous zinc ion capacitors (ZICs).[6] As for the carbon cathode materials, they can deliver high power density and lifespan due to the fully reversible Zn^{2+} adsorption/desorption. However, they generally encounter unsatisfactory Zn^{2+} storage capacity owing to insufficient adsorption/desorption sites.[7] Hence, the key to enhancing the Zn storage capacity lies in engineering the carbonaceous materials to accommodate the density of Zn^{2+}.

To enhance the Zn^{2+} storage capability, diverse parameters of carbonaceous materials such as conductivity, surface functionality, specific surface area (SSA), pore size, and pore volume should be taken into account.[8] According to the relationship between capacitance (C) and accessible surface area (A), and the average distance of ionic charge center to electrode surface (d) (expressed by $C = \epsilon_0\epsilon_r A/d$, where ϵ_0 is the permittivity of the vacuum and ϵ_r is the relative dielectric constant), increasing A and reducing d are the direct approaches to enhance C. Notably, pores with sizes equivalent to the charge carriers will render optimal capacity and energy density.[9] In aqueous electrolyte, Zn^{2+} forms solvation structures with water molecules, varying in size from 0.15 to 0.86 nm. The primary solvation structure, $[Zn(H_2O)_6]^{2+}$, is characterized by a large size of 0.86 nm.[10] Apparently, the solvated $[Zn(H_2O)_6]^{2+}$ has difficulty in infiltrating pores smaller than itself due to the high hydration free energy, resulting in low charge density (**Scheme 1a**). However, pores much larger than $[Zn(H_2O)_6]^{2+}$ correspond to large d value and small A value

X. Li, C. Cai, P. Hu, P. Wu, H. Fan, Z. Chen, L. Zhou, L. Mai
State Key Laboratory of Advanced Technology for Materials Synthesis and Processing
Wuhan University of Technology
Wuhan 430070, P. R. China
E-mail: liangzhou@whut.edu.cn; mlq518@whut.edu.cn
X. Li, B. Zhang, H. J. Fan
School of Physical and Mathematical Sciences
Nanyang Technological University
Singapore 637371, Singapore
E-mail: fanhj@ntu.edu.sg
L. Zhou, L. Mai
Hubei Longzhong Laboratory
Wuhan University of Technology (Xiangyang Demonstration Zone)
Xiangyang, Hubei 441000, P. R. China

The ORCID identification number(s) for the author(s) of this article can be found under https://doi.org/10.1002/adma.202400184

DOI: 10.1002/adma.202400184

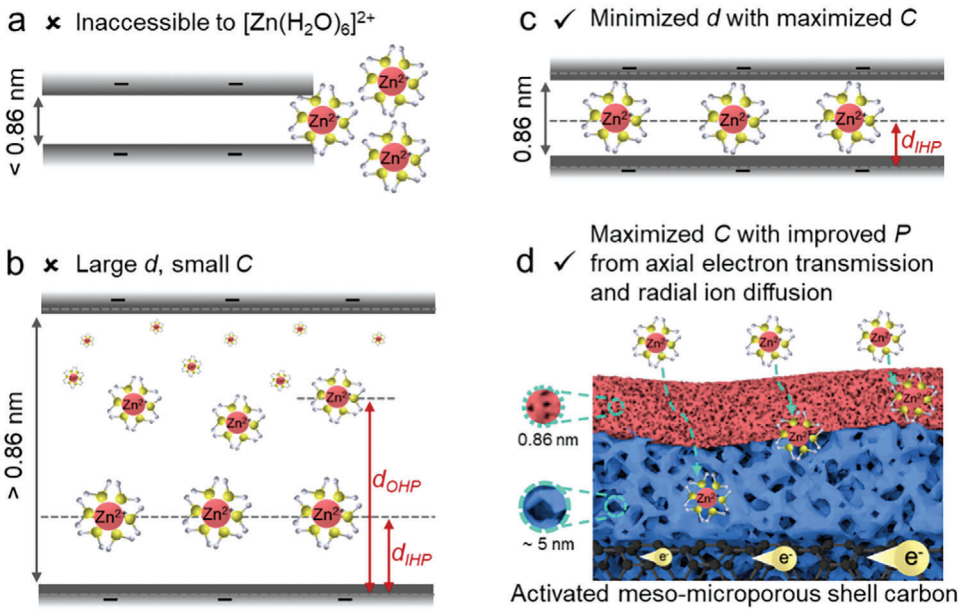

Scheme 1. Design rational of gradient-pore carbon electrode. $[Zn(H_2O)_6]^{2+}$ residing in pores with distance between adjacent pore walls a) less than 0.86 nm, b) greater than 0.86 nm, and c) equal to 0.86 nm (diameter of $[Zn(H_2O)_6]^{2+}$). d) A comprehensive illustration of $[Zn(H_2O)_6]^{2+}$ entering into MMSC-A.

for double-layer formation, leading to an indispensable loss in charge density (Scheme 1b).[11] Hence, a strategic construction of functional carbonaceous materials with pore sizes comparable to that of $[Zn(H_2O)_6]^{2+}$, coupled with high SSA, is beneficial to high-density Zn^{2+} storage (Scheme 1c). On the other hand, although narrow pores with an optimal size of 0.86 nm will contribute to the maximized *C* and high energy density, they may compromise the power density. To further optimize the carbonaceous materials for high energy storage and power output, it is necessary to increase the volume of narrow but short pores. In this context, devising fibrous structures with dual pathways for axial electron transmission and radial ion diffusion, in conjunction with gradient meso-micropores, holds great promise (Scheme 1d). There are scarce reports on fibrous carbon electrodes with gradient pores for metal-ion capacitors. On another note, despite the broad interests in ZICs, very few studies engage in situ techniques to investigate the charge storage mechanism in carbonaceous materials within small-size pores.

The objective of this study is to engineer gradient porous carbon materials for enhancing the charge storage density and to elucidate the associated storage mechanism through multifold in situ means. We constructed activated meso-microporous shell carbon (MMSC-A) nanofibers via a one-pot surfactant-free self-assembly strategy. The enhancement in charge storage density relies on the following aspects: i) The large SSA (3823 $m^2\ g^{-1}$), mainly contributed by micropores, and ultrahigh pore volume (3.01 $cm^3\ g^{-1}$), primarily ascribed to mesopores, establish abundant sites for Zn^{2+} storage. ii) The size compatibility between pore and hydrated ions promotes the monolayer arrangement of $[Zn(H_2O)_6]^{2+}$ in pores, showcasing a small *d* value with a large *C*. The 0.86 nm pore features a low adsorption energy of −0.89 eV toward $[Zn(H_2O)_6]^{2+}$, facilitating the adsorption and storage of Zn^{2+}. iii) The abundant oxygen species on the carbon surface participate in the reversible chemical adsorption of Zn^{2+}, thereby increasing the charge density at the unit surface area. iv) Finally, the designed MMSC-A features ion/electron dual conduction pathways and favorable wettability toward electrolyte, aiding in the ion transport kinetics within the meso-micropores. The above traits endow MMSC-A with a capacity of 257 mAh g^{-1} and an energy of 199.8 Wh kg^{-1} at a power of 77.6 W kg^{-1}, with a capacity retention of 95.4% at 2 A g^{-1} after 10 000 cycles. Importantly, the detailed electrochemical reactions and charge storage mechanism within this gradient-pore carbon fibers have been revealed by theoretical calculation and various in situ and ex situ characterizations, including Raman, ATR-FTIR, XRD, and XPS. This study provides note only new route for constructing functional carbonaceous materials with high charge storage density, but also insights to the charge storage mechanism for ZICs.

2. Results and Discussions

The preparation of MMSC-A is elucidated in **Figure 1a**. Initially, the multilayer core–shell structured CNT@organosilica@APF nanofibers were obtained through a one-pot surfactant-free self-assembly synthesis driven by H-bond in aqueous solution, avoiding laborious layer-by-layer coating and the requirement for costly organic solvent.[12] Among them, organosilica derived from the hydrolytic polymerization of vinyltrimethoxysilane (VTMS), served as mesoporous shell carbon source by template removing, facilitating ion mobility (Figure 1b). 3-aminophenol/formaldehyde (APF) generated through phenolic condensation, acted as narrow but short microporous carbon shell source, providing abundant active sites (Figure 1c). CNT was employed as the nucleation seed, structure-directing agent and conductive path to realize the tri-function of lowering nucleation barrier, building 3D network, and facilitating electron

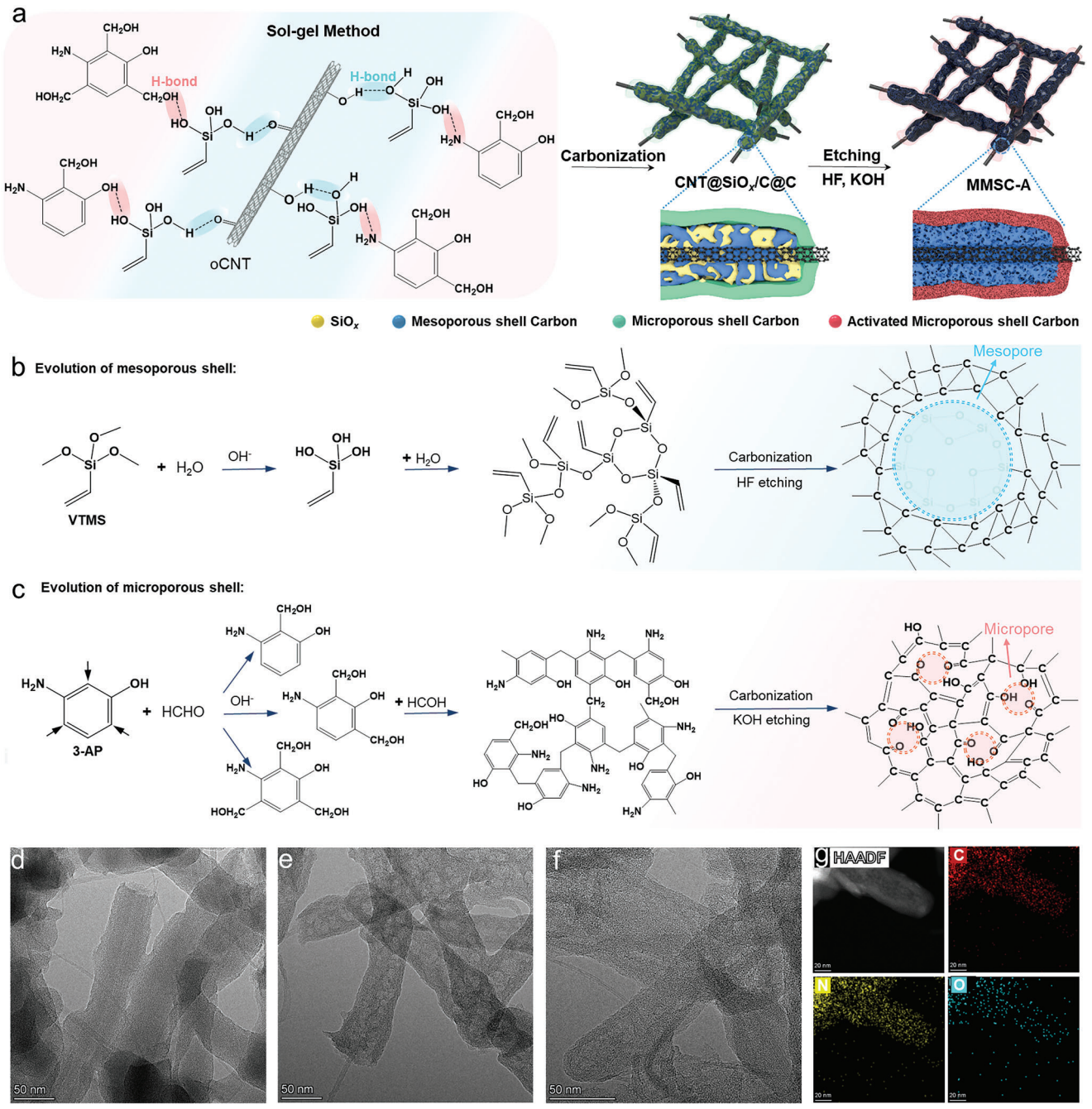

Figure 1. Formation of gradient pores. a) The chemical assembly of multilayer core–shell structure driven by H-bond with subsequent carbonization and etching. b) Schematic of the evolution of mesoporous shell carbon. c) The evolution of microporous shell carbon. TEM images of d) CNT@SiO_x/C@C, e) MMSC, and f) MMSC-A. g) HAADF-STEM image and the corresponding EDS elemental mappings of MMSC-A.

transport.[13] Subsequent steps involve carbonization to obtain CNT@SiO_x/C@C, followed by HF etching to acquire MMSC by removing silicon oxide in SiO_x/C. The final activation step tailors the pore structure and surface chemistry to yield MMSC-A with optimized properties.

Microscopy characterizations reveal the beaded structure of CNT@organosilica nanofibers (Figure S1a,b, Supporting Information). Subsequent coating with APF results in an increased diameter of CNT@organosilica@APF (Figure S1c,d, Supporting Information). The core–shell structure of CNT@SiO_x/C@C (Figure 1d) is evident, comprising an innermost CNT core, an intermediate SiO_x/C shell, and an outermost microporous carbon shell. This structural configuration is supported by energy-dispersive X-ray spectroscopy (EDS) elemental mappings (Figure S2, Supporting Information). The MMSC possesses a well-defined intermediate mesoporous carbon shell with pore sizes around 5 nm (Figure 1e; and Figure S3, Supporting Information). As for the MMSC-A, the structural optimization (Figure 1f,g)

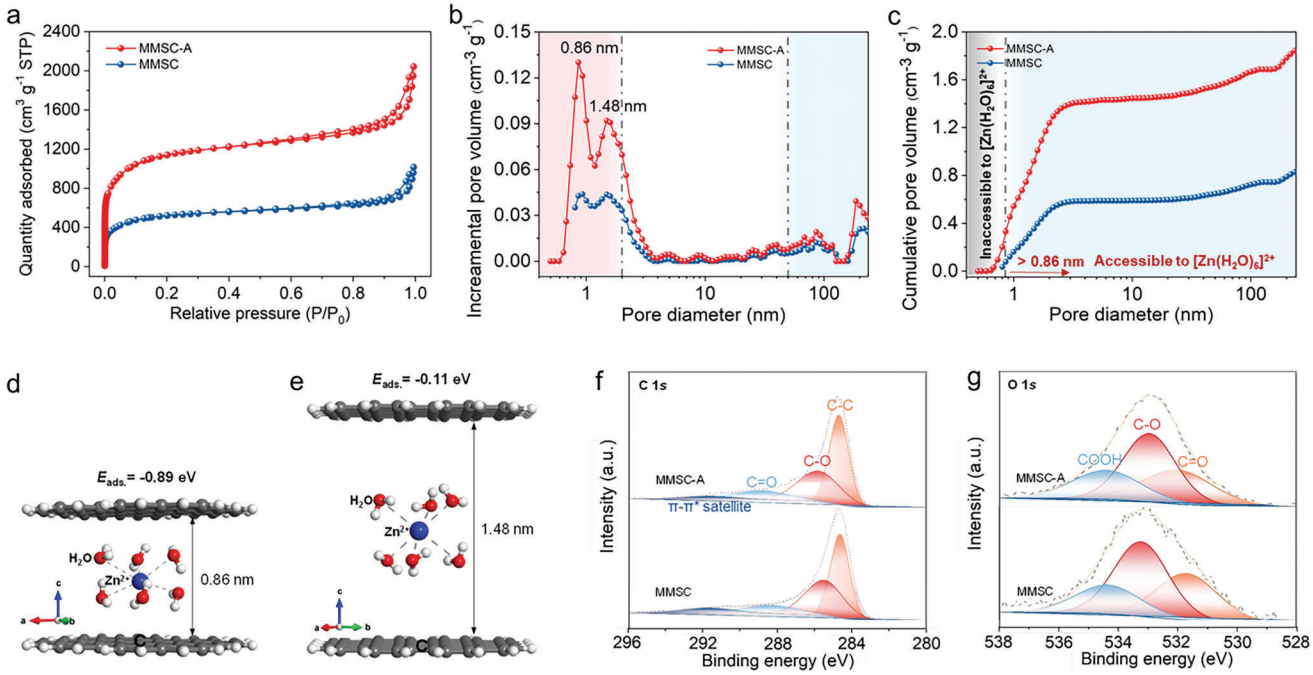

Figure 2. Structural characterization of MMSC-A and MMSC. a) N_2 adsorption/desorption isotherms. b,c) Corresponding pore size distributions. The optimized structures of $Zn(H_2O)_6^{2+}$ adsorbed on double-layer graphene with layer distances of d) 0.86 nm and e) 1.48 nm for the NLDFT calculation of adsorption energy. f,g) High resolution C1s and O1s spectra.

promotes a fine-tuned intermediate mesoporous shell and a reduction in thickness of the outermost microporous carbon shell. This modification may facilitate electrolyte permeability and enhances charge storage. Thermogravimetry coupled with mass spectrometry (TG-MS) monitors mass changes and gas release during the pyrolysis process in an inert atmosphere (Figure S4, Supporting Information). The continuous mass loss is primarily ascribed to CO release from rupture of the oxygen-silicon bonds at the SiO_x/C interface. The evident reduction in mass below 100 °C can be attributed to the evaporation of capillary water and organic small molecules. Mass loss at 320 °C indicates the decomposition of the outermost resin shell corresponding to CH_3^+ (m/z = 15), H_2O (m/z = 18), CO (m/z = 28), and CH_3OH (m/z = 32).[14] The absence of substantial losses up to 800 °C affirms the suitability of the carbonization temperature. X-ray diffraction (XRD) patterns of MMSC and CNT@SiO_x/C@C display two broad peaks at ≈24° and 43°, relating to the (002) and (100) planes of amorphous carbon, respectively (Figure S5a, Supporting Information).[15] The pronounced diffraction intensity of MMSC-A at ≈10° implies the well-developed microporous structure. Raman spectra show the peak at ≈1360 cm^{-1} (D-band), attributing to sp^3-type defective carbon. Peaks at 1580 (G-band) and 2700 cm^{-1} (2D-band) correspond to sp^2-type graphitic carbon (Figure S5b, Supporting Information).[16] The higher I_D/I_G ratio observed in MMSC-A compared to MMSC signifies the evolving micropores, consistent with XRD results. The slight divisive tendency of G peaks is associated with the sp^2-type carbon present in both the CNT core and the carbon shell.

To assess the microtexture of the prepared samples, N_2-sorption was executed (**Figure** 2a–c; and Figure S6, Supporting Information). The typical type-I isotherms exhibit substantial N_2 adsorption at $P/P_0 < 0.1$ with a minor hysteresis loop at P/P_0 = 0.55–0.95, demonstrating the predominance of micropores accompanied by partial mesopores.[17] Compared to CNT@SiO_x/C@C, the ≈5 nm pore observed in MMSC is a result of the silica removal. The well-developed micropores confer MMSC-A the larger SSA and pore volume (3823 m^2 g^{-1}, 3.01 cm^3 g^{-1}), more than twice those of MMSC (1745 m^2 g^{-1}, 1.48 cm^3 g^{-1}), and over three times those of CNT@SiO_x/C@C (1035 m^2 g^{-1}, 0.95 cm^3 g^{-1}), implying more active sites and a larger accommodation space for Zn^{2+} storage (Table S1, Supporting Information). Nonlocalized density function theory (NLDFT) pore size distribution curves exhibit consistent pore sizes of all samples at 0.86 and 1.48 nm, reflecting stable structural evolution benefited from high corrosion resistance of CNT@SiO_x/C@C. The minimal change in size is attributed to the inherent thermostability of the microporous shell carbon precursor resin and the rigid support provided by the mesoporous shell carbon precursor of organosilica. For aqueous ZICs, $[Zn(H_2O)_6]^{2+}$ is the primary charge carrier with a size of 0.86 nm.[10c] The main pore size of 0.86 nm in MMSC-A is accessible to single hydrated $[Zn(H_2O)_6]^{2+}$, which renders a dense arrangement of $[Zn(H_2O)_6]^{2+}$ on active surfaces for maximizing Zn^{2+} storage.

Insights into the interaction between pore size and charge carrier are obtained through density functional theory (DFT) calculations (Figure 2d,e; and Table S2, Supporting Information). As the NLDFT pore size distribution result is based on the specific slit pore model, the double-layer graphene structure is employed. Given the smaller size of SO_4^{2-} (0.76 nm) in comparison to $[Zn(H_2O)_6]^{2+}$ (0.86 nm), only the adsorption energy of $[Zn(H_2O)_6]^{2+}$ on double-layer graphene with layer distance of 0.86 and 1.48 nm is taken into consideration.[18] Then the

corresponding adsorption energies for $[Zn(H_2O)_6]^{2+}$ are −0.89 and −0.11 eV, respectively. The negative adsorption energy indicates the favorable structure of MMSC-A for the storage of $[Zn(H_2O)_6]^{2+}$. The stronger affinity of 0.86 nm pores enables them to capture a larger quantity of $[Zn(H_2O)_6]^{2+}$, ultimately enhancing the Zn^{2+} storage density.

X-ray photoelectron spectroscopy (XPS) was conducted to detect surface chemical composition. The spectra suggest the coexistence of C, O, and N elements in all samples (Figure S7a–c, Supporting Information). CNT@SiO_x/C@C displays a low Si content of 3.78 at% on the outermost microporous carbon shell, indicating the successful coating (Figure S7a, Supporting Information). A minor peak at 685.7 eV corresponds to 1*s* orbit of F from HF etching (Figure S7b, Supporting Information). The KOH activation process removes most nitrogen components, creating N vacancies and introduces O species, which are beneficial for Zn^{2+} storage. The oxygen functional group exhibits an initial decrease followed by an increase, with percentages of 9.17 at%, 4.03 at%, and 10.77 at% for CNT@SiO_x/C@C, MMSC, and MMSC-A, respectively (Figure S7d, Supporting Information). The C1*s* spectra can be decomposed into four components: C—C (284.8 eV), C—O (285.9 eV), C═O (289.0 eV), and π–π^* satellite (291.4 eV) (Figure 2f; and Figure S8a, Supporting Information). The N 1*s* spectra can be resolved into four peaks (Figures S8b and S9, Supporting Information), attributing to pyridinic nitrogen (N-6, 398.2 eV), pyrrolic nitrogen (N-5, 400.7 eV), graphitic nitrogen (N-Q, 403.1 eV), and oxidized-N (N—O, 406.1 eV). The O 1*s* spectra can be fitted into three components: C═O (531.9 eV), C—O (533.2 eV), and COOH (534.4 eV) (Figure 2g; and Figure S8c, Supporting Information).[19] The C—O is the main component (Figure S10, Supporting Information) and the reversible conversion between C—O and C═O will enable efficient desorption and adsorption of Zn^{2+}.[20] The wettability at electrode/electrolyte interface was characterized by dynamic contact angle measurements (Figure S11, Supporting Information). The initial contact angle of MMSC-A toward $ZnSO_4$ is 20.4°, which decreases to 11.8° after 4 min. While MMSC also exhibits descent wettability, its contact angle after 4 min remains at a relatively higher value of 45.9°, which can be attributed to its lower specific surface area and fewer surface functional groups. The optimal pore size and exceptional wettability will collectively benefit electron/ion transport for Zn^{2+}. Consequently, Zn^{2+} ions efficiently access all the active surface area inside MMSC-A, as demonstrated by high-angle annular dark-field scanning transmission electron microscopy (HAADF-STEM) and corresponding EDS elemental mappings (Figure S12, Supporting Information).

Although the pore structure and surface chemistry of MMSC-A have been elucidated through ex situ methods, the real-time observation of their impact on Zn^{2+} storage through in situ means has been scarce. In the present study, in situ Raman spectroscopy (**Figure 3a**) provides insight into subtle electrochemical doping effect of MMSC-A during charge and discharge processes, highlighting the size compatibility between pores and charge carriers.[21,18] Upon the initial charging to 1.8 V and subsequent discharging to 0.2 V, the slight increase in intensity and broadening of the D- and G-bands is observed. This phenomenon can be attributed to the interaction between carbon walls with SO_4^{2-} and $[Zn(H_2O)_6]^{2+}$ (Equations (1) and (2)). Notably, during discharge to 0.2 V, the effect becomes more pronounced, attributable to larger size of solvated $[Zn(H_2O)_6]^{2+}$ (0.86 nm) in comparison to SO_4^{2-} (0.76 nm)), along with the chemical adsorption of oxygen species onto $[Zn(H_2O)_6]^{2+}$. The unaltered positions of the D- and G-bands throughout the electrochemical process suggest the absence of ion insertion/extraction processes (Figure S13a, Supporting Information).[22] Instead, the process exclusively involves ion adsorption/desorption, which is favorable for cycling performance. At 1.8 V, the rise in I_D/I_G value correlates with the release of $[Zn(H_2O)_6]^{2+}$ from internal occupied defects. The additional increase in defects at 0.2 V is associated with the chemical adsorption of $[Zn(H_2O)_6]^{2+}$, which plays a significant role in increasing carbon material defects (Figure S13b, Supporting Information).[23]

In situ attenuated total reflection-Fourier transform infrared (ATR-FTIR) spectroscopy was employed to study the dynamic changes of carbon surface functional groups occurring at the electrode/electrolyte interface (Figure 3b). The peak at 700 cm^{-1} corresponds to the in-plane bending vibration of CO—H, which exhibits consistent variations with O—H stretching vibration at 3350 cm^{-1}.[24] Upon charging to 1.8 V, a notable increase in O—H peaks is observed, which can be attributed to the desorption of Zn^{2+}, causing the breakage of chemical adsorption bonds involving C—O—Zn (Equation (3)). Additionally, during discharging to 0.2 V, the slight enhancement of O—H peaks can be observed, which is attributed to the active participation of H^+ with C═O in the reaction to form C—OH (Equation (4)). The inverse trend observed in C—O peak[25] at 1081 cm^{-1} indicates the highly reversibility of Zn^{2+} adsorption/desorption. When discharged to 0.2 V, the adsorption of Zn^{2+} by C═O leads to the formation of C—O—Zn, resulting in a stronger C—O vibration peak. The peak observed at 1646 cm^{-1} is associated with the vibration of C═C, and the increased intensity signifies an augmentation in defect density.[25] In alignment with the in situ Raman spectroscopy results, the increase in defects is detected at both the maximum positive polarization and negative polarization states. The vibration at 3155 cm^{-1} is attributed to the stretching vibration of ═C—H,[26] which originates from the O═C—H group (Figure S14a, Supporting Information). In comparison to MMSC, MMSC-A exhibits abundant surface oxygen and minimal nitrogen. This aligns with XPS analysis and suggests that surface pseudocapacitance primarily arises from the oxygen species (Figure S14b, Supporting Information). The increase in ═C—H vibration peaks is notable at 1.8 V and becomes the second highest at 0.2 V with an opponent trend to that of C—O peak, providing additional support for the highly reversible conversion between C═O and C—O—Zn.

The participation of H^+ in the reaction is discerned through the intensity fluctuations in the CO—H bond, as observed by in situ ATR-FTIR analysis. Moreover, in situ XRD measurement (Figure 3c) provides further evidence of H^+ involvement by observing the precipitation/dissolution of $Zn_4SO_4(OH)_6{\cdot}5H_2O$ at 32.6° (Equation (5)).[23] Ex situ SEM analysis illustrates structural evolution on the Zn anode surface in five different states (Figure S15, Supporting Information). In contrast to the original zinc anode, the surface at various potentials exhibits increased roughness without dendrite formation, which is attributed to the highly reversible Zn deposition/stripping, benefiting long-term cyclic stability.[27] Ex situ XPS was conducted to probe the chemical states of MMSC-A across five distinct charge/discharge

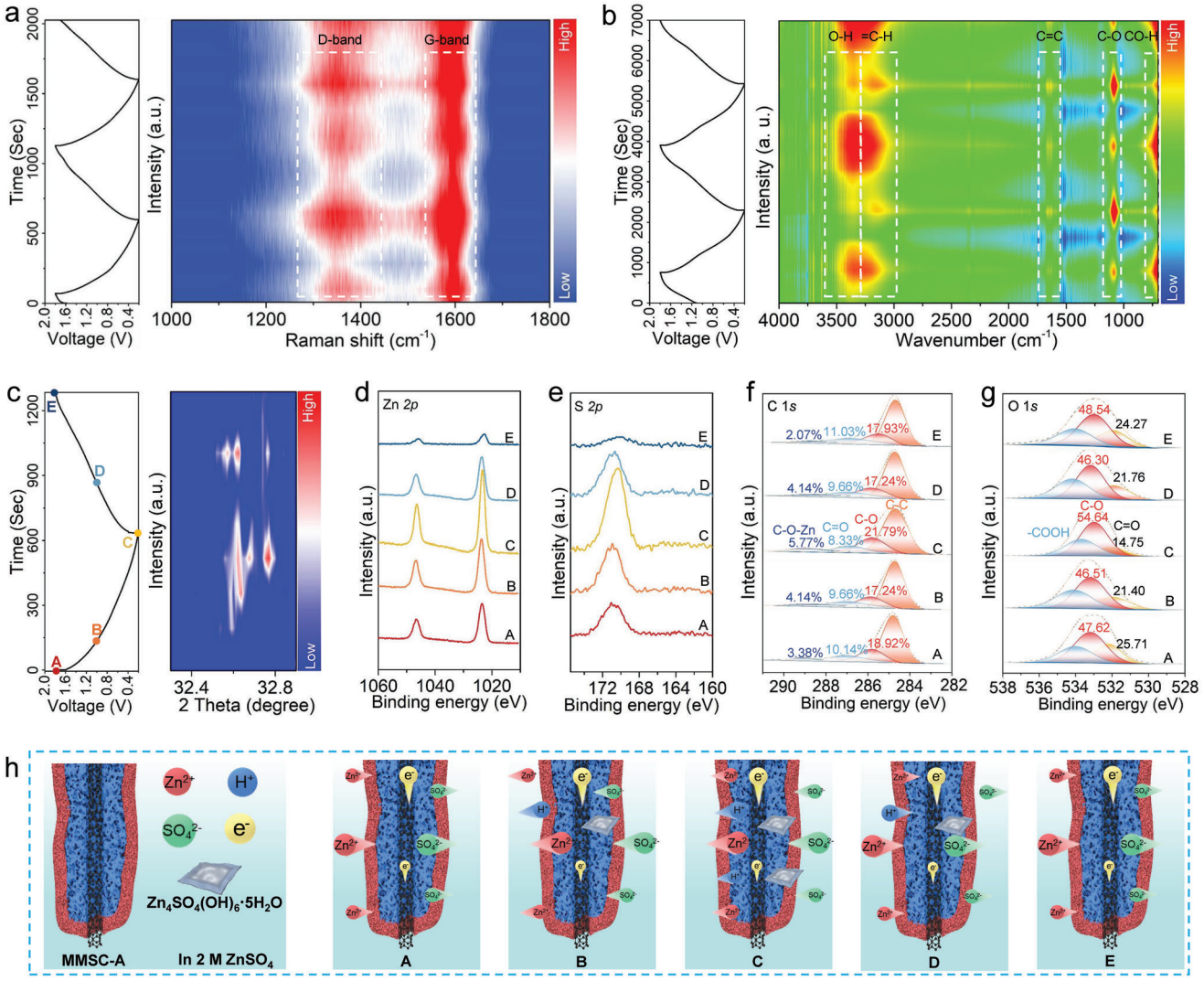

Figure 3. In situ characterization and charge-storage mechanism for MMSC-A. a) In situ Raman spectra, b) in situ ATR-FTIR spectra, c) in situ XRD measurements, and d–g) ex situ XPS survey spectra during 1st cycle of charge and discharge in 2 mol L^{-1} $ZnSO_4$ electrolyte. h) Schematic illustration of the charge storage mechanism inferred from the above analysis.

states. During the initial charging to 1.8 V (State A), a noticeable intensity of Zn 2*p* is observed, indicating favorable wettability and spontaneous adsorption between $[Zn(H_2O)_6]^{2+}$ and MMSC-A (Figure 3d). As the discharge proceeds to 0.2 V (State C), the intensity of Zn 2*p* reaches its peak, highlighting substantial chemical adsorption of Zn^{2+} during deep discharge. Upon subsequent recharging to 1.8 V again (State E), the intensity of Zn 2*p* diminishes as Zn^{2+} ions retreat from pores (Equation (6)). At State A, a notable adsorption of SO_4^{2-} occurs with a high intensity of S 2*p* (Figure 3e). Subsequently, the intensity reaches its maximum due to the precipitation of $Zn_4SO_4(OH)_6{\cdot}5H_2O$,[28] consistent with the results from in situ XRD. The dissolution of $Zn_4SO_4(OH)_6{\cdot}5H_2O$ with elevated potential is manifested by the gradual decrease in intensity. To provide further evidence for the reversible chemisorption of Zn^{2+}, the ex situ C 1*s* XPS result is deconvoluted into four components (Figure 3f). At 0.2 V, the C═O bond exhibits the lowest intensity, while the C—O—Zn and C—O bonds reach their highest levels, corresponding to the chemisorption of C═O with Zn^{2+} to form C—O—Zn and the interaction of C═O with H^+ (Equation (7)). Meanwhile, the O 1*s* spectrum is resolved into three components and the variation in content of C═O and C—O exhibits opposite trends (Figure 3g). The alignment with the results from the C 1*s* spectrum reveals the high reversibility of the C═O and C—O conversion for the Zn^{2+} storage.[8c]

On the basis of above in situ and ex situ characterizations complemented by theoretical calculation, we may elucidate the charge storage mechanism of MMSC-A cathode in 2 M $ZnSO_4$ electrolyte. The possible reactions occurring on the MMSC-A cathode can be summarized as follows.[5c,8c]

Physical adsorption/desorption

$$C + Zn^{2+} \leftrightarrow C||Zn^{2+} \quad (1)$$

$$C||SO_4^{2-} \leftrightarrow C + SO_4^{2-} \quad (2)$$

Reversible chemical adsorption/desorption

$$C=O + Zn^{2+} + 2e^- \leftrightarrow C-O-Zn \quad (3)$$

$$C=O + H^+ + e^- \leftrightarrow C-O-H \quad (4)$$

Precipitation/dissolution

$$4Zn^{2+} + SO_4^{2-} + 6OH^- + 5H_2O \leftrightarrow Zn_4SO_4(OH)_6 \cdot 5H_2O \quad (5)$$

Reversible electrochemical interaction

$$C\cdots O + Zn^{2+} + 2e^- \leftrightarrow C\cdots O\cdots Zn \quad (6)$$

$$C\cdots O + H^+ + e^- \leftrightarrow C\cdots O\cdots H \quad (7)$$

With these reactions, the charge storage mechanism during the charging and discharging process is summarized in Figure 3h. First, the alignment between pore sizes and charge carriers has been verified by NLDFT pore size distribution, theoretical calculation, and in situ Raman spectroscopy. This alignment, coupled with high SSA and ample pore volume, is beneficial for high density Zn^{2+} storage. Second, the traditional coadsorption mechanism of Zn^{2+} and SO_4^{2-}, which has been verified by in situ Raman spectra, occurs in the low and high potential regions, respectively. Third, the involvement of H^+ in the reaction has been observed by in situ FTIR spectra and XRD measurements, with H^+ bonding at low potential and releasing at high potential, resulting in dynamic local pH changes. Finally, the reversible chemical adsorption of Zn^{2+} has been revealed by in situ FTIR and ex situ XPS results. The high reversibility of C═O and C—O conversion to form C—O—Zn introduces pseudocapacitance and contributes to the total charge density.

Aqueous ZICs were assembled by employing MMSC-A as the cathode material and Zn foil as the anode. As discussed above, the reactions involve reversible plating/stripping of Zn at the anode, rapid adsorption/desorption of Zn^{2+} and SO_4^{2-}, and reversible precipitation/dissolution of intermediate species of $Zn_4SO_4(OH)_6{\cdot}5H_2O$ at the cathode (**Figure 4a**). Cyclic voltammetry (CV) curves at 1 mV s^{-1} exhibit a rectangle-like shape with characteristic redox peaks for both MMSC-A and MMSC based devices (Figure S16, Supporting Information). This suggests that the charge-storage mechanisms are associated with pseudocapacitive behavior, a phenomenon that is also reflected by the linear galvanostatic charge–discharge (GCD) curves (Figure 4b). The integrated area of MMSC-A is nearly twice that of MMSC. The discharge capacities calculated from the GCD curves conducted at 0.1 A g^{-1} are 257.3 and 150.1 mAh g^{-1} for MMSC-A and MMSC, respectively (Figure 4b). Hence, the former delivers higher specific capacity than the later. Regarding rate performance, it is a fact that micropores suffer from poor rate performance due to kinetics limit.[29] Hence, the incorporation of intermediate mesoporous shell is expected to benefit the ion transport. A reversible capacity of 68 mAh g^{-1} is achieved at 20 A g^{-1} (Figure 4c; and Figure S17, Supporting Information). The maximum specific capacities achieved by the MMSC-A cathode-based ZIC surpass those reported in recent literature (Figure 4d).[30,1d] Moreover, the quasisolid-state device based on MMSC-A renders a storage capability of 245 mAh g^{-1} at 0.2 A g^{-1} (Figure 4e). This improved Zn^{2+} storage performance can be attributed to the pore structure that is comparable to the size of the ions, which minimizes the Debye length and lowers the adsorption energy.

For potential practical applications, the specific capacity and energy density of MMSC-A ZIC at 0.5 A g^{-1} with varying mass loadings (0.96–11.58 mg cm^{-2}) are explored. When the loading is below 5.79 mg cm^{-2}, no discernible voltage drop is observed (Figure 4f; and Figure S18, Supporting Information). An further increase in mass loading results in significant capacity drop due to inefficient ion transport, a phenomenon well-documented in nanoconfined carbon materials. In our design, the 1D structure with CNT backbone and gradient pore shells may have streamlined the ion transport. However, further holistic optimization of the electrode structure is still necessary to achieve high power performance.

We analyze the kinetic property of the devices in two ways. First, the capacitive and diffusion contributions to the capacity can be estimated by fitting the CV curves using the empirical equation $i = av^b$, where i represents the peak current, v denotes the sweep rate, and a and b are constants.[28] A b value of 0.5 suggests diffusion-controlled behavior, whereas the b value of 1.0 indicates the capacitive-dominating behavior. The CV curve of MMSC-A shows no significant deformation as the scanning rate increases from 1 to 20 mV s^{-1}, illustrating its favorable kinetics (Figure S19, Supporting Information). Specifically, the calculated b values for the MMSC-A cathode are 0.77 and 0.72 for the redox peaks, indicative of a mixed charge storage process (Figure S20a, Supporting Information). Our b values are relatively small compared to the most porous carbon electrodes which give b values close to 0.9. This discrepancy highlights the size compatibility between pores and hydrated ions, which promote a capacity enhancement while compromising charging kinetics. Further kinetic analysis[31] reveals that the proportion of the capacitive contribution to the total capacity over the diffusion-controlled process is 52.7% at 2 mV s^{-1} and surges to 93.7% when the scan rate increases by ten times (Figure S20, Supporting Information). Second, the Nyquist plot in electrochemical impedance spectroscopy (EIS) also indicates more efficient charge transfer for the MMSC-A device than MMSC as benefited from the optimized pore structure (Figure S21, Supporting Information). The equation $C(\omega) = C'(\omega) + jC''(\omega)$ calculated from EIS test is employed to analyze the variations in capacitance, where $C(\omega)$ is the total capacitance, $C'(\omega)$ and $C''(\omega)$ denote the real and imaginary capacitance, respectively.[32] The MMSC-A exhibits a higher $C'(\omega)$ of 73 mF, over twice that of MMSC. Consistently, the MMSC-A device has higher $C''(\omega)$ and smaller time constant. This result also reveals fast Zn^{2+} diffusion kinetics in MMSC-A.

According to the Ragone plot, the MMSC-A based ZIC shows an energy of 199.8 Wh kg^{-1} at the power of 77.6 W kg^{-1}, surpassing most of reported carbonaceous materials in ZICs (Figure 4g).[8c,30a,b,h] Assuming the active material constitutes one-fourth of the device total mass,[33] our MMSC-A based ZIC device can deliver an energy density of 50 Wh kg^{-1}. Two ZIC devices assembled in series illuminate a "Carbon" light bulb comprising 99 red light emitting diodes. Furthermore, the MMSC-A and MMSC device retain 95.4% and 90.8% of their initial

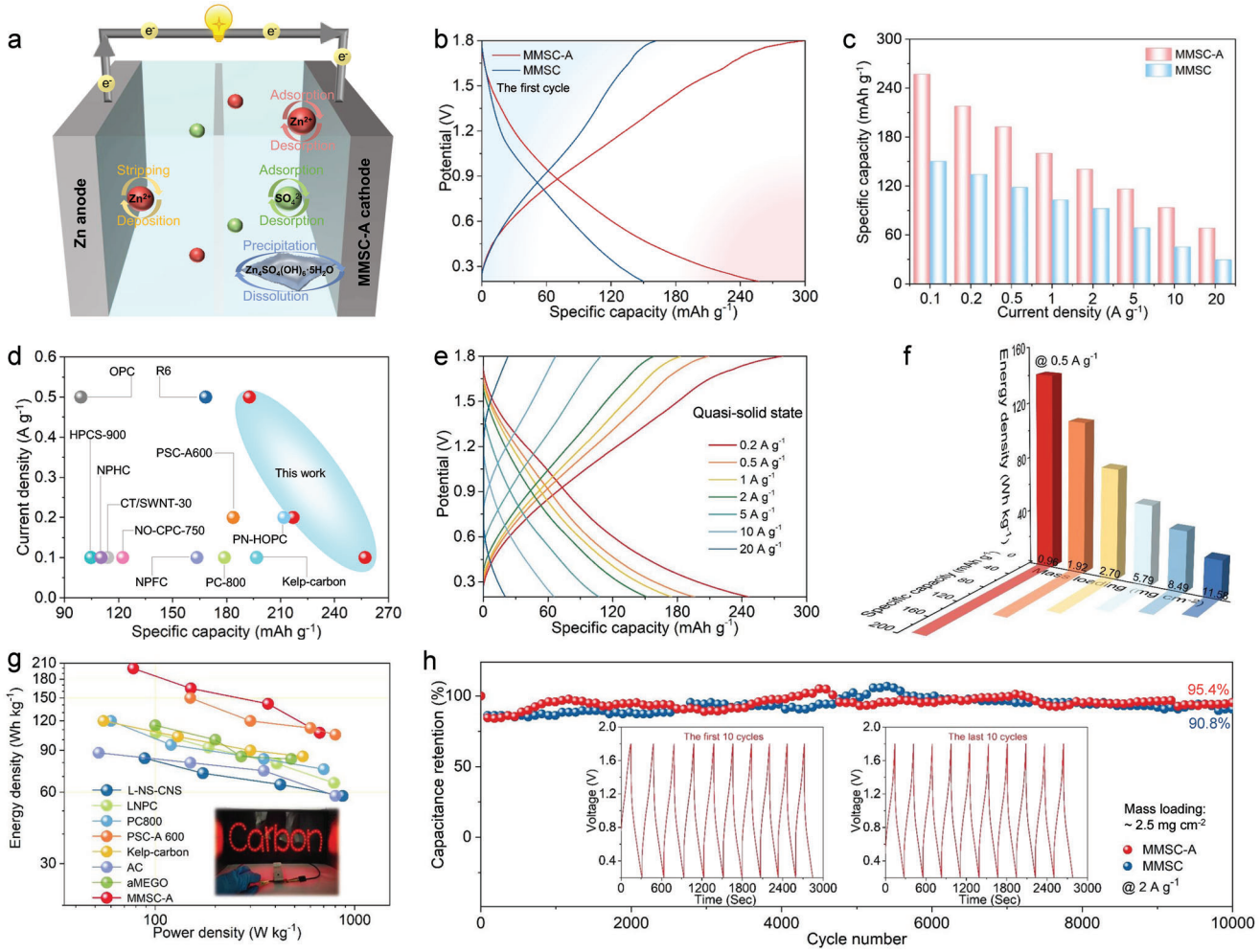

Figure 4. Electrochemical behaviors of Zn-ion capacitors (ZICs). a) Schematics of the structure and working mechanism of ZICs. b) GCD curves of ZICs made from MMSC-A and MMSC at 0.1 A g^{-1}. c) Comparison of specific capacities at various current densities. d) Comparison to various cathode ZICs in literature.[30,1d] e) GCD curves of MMSC-A quasisolid-state ZICs at different current densities. f) Energy densities and specific capacities of MMSC-A ZIC at 0.5 A g^{-1} as a function of mass loadings. g) Ragone plot in comparison to state-of-the-art carbon cathodes based ZICs. The calculation is based on mass of the active carbon materials only. The inset shows 99 red LEDs are illuminated by two ZIC devices in series. h) Capacity retentions of both electrodes at 2 A g^{-1}. Insets are the GCD curves of the first and last ten cycles.

capacity at 2 A g^{-1} after 10 000 cycles, respectively (Figure 4h). The GCD profiles for the initial and final ten cycles maintain the nearly linear and symmetric shapes with negligible degradation. As the characteristic property of a capacitor device, the CV curves of quasisolid-state device based on MMSC-A exhibit rectangle-like shape without significant deformation as the scanning rate increases from 2 to 20 mV s^{-1} (Figure S22a, Supporting Information). When the current density exceeds 5 A g^{-1}, the specific capacity undergoes a sharp drop (Figure S22b, Supporting Information), which can be explained by the fact that the micropores and small-sized mesopores are less efficient for ion transport than the large-sized mesopores. The output voltage/current of device can be enhanced through series/parallel connection to fulfill the energy/power requirement (Figure S23, Supporting Information). Moreover, the device was flexed over a range from 0° to 180° with capacity retention close to 100% (Figure S24, Supporting Information). The improved comprehensive electrochemical performance, coupled with flexible and durable operation, positions MMSC-A as a promising candidate for high-performance ZICs.

3. Conclusion

We have designed a micro-mesoporous carbon nanofibers cathode and achieved significantly enhanced charge storage capacity of hybrid zinc ion capacitor. This results from a leveraged gradient-pore 1D electrode structure, in which the aligned pores with appropriate sizes facilitate efficient ion access without ion sieving effect, and the oxygen-rich functional groups render surface redox reactions. A series of in situ characterizations reveals that the Zn^{2+} storage within small-sized pores involves several mechanisms, including the traditional coadsorption mechanism of Zn^{2+} and SO_4^{2-}, participation of H^+ in reaction with additional pseudocapacitance, and high reversibility of surface C═O and C—O conversion reactions with Zn^{2+}. Benefiting from high surface areas and abundant affinity charge storage sites, the

MMSC-A electrode presents a high specific capacity of 257 mAh g^{-1}, an energy density of 199.8 Wh kg^{-1} at a power density of 77.6 W kg^{-1}, and a capacity retention of 95.4% after 10 000 cycles. This study provides insights into designing and working mechanism of porous carbon cathodes for high charge density hybrid metal-ion capacitors.

Supporting Information

Supporting Information is available from the Wiley Online Library or from the author.

Acknowledgements

X.Y.L. and C.C.C. contributed equally to this work. This work was supported by the National Natural Science Foundation of China (No. 52072283), the National Key Research and Development Program of China (No. 2020YFA0715000), the National Natural Science Foundation of China (No. 52127816), and the program of China Scholarship Council (No. 202306950008).

Conflict of Interest

The authors declare no conflict of interest.

Data Availability Statement

The data that support the findings of this study are available from the corresponding author upon reasonable request.

Keywords

charge storage mechanism, gradient pores, porous carbon, reversible chemical adsorption, zinc ion capacitor

Received: January 4, 2024
Revised: February 8, 2024
Published online: February 19, 2024

[1] a) E. Pomerantseva, F. Bonaccorso, X. Feng, Y. Cui, Y. Gogotsi, *Science* **2019**, *366*, eaan8285; b) P. Simon, Y. Gogotsi, *Nat. Mater.* **2020**, *19*, 1151; c) X. Wang, M. Salari, D. Jiang, J. C. Varela, B. Anasori, D. J. Wesolowski, S. Dai, M. W. Grinstaff, Y. Gogotsi, *Nat. Rev. Mater.* **2020**, *5*, 787; d) J. Huang, Y. Xie, Y. You, J. Yuan, Q. Xu, H. Xie, Y. Chen, *Adv. Funct. Mater.* **2023**, *33*, 2213095.

[2] a) P. Simon, Y. Gogotsi, B. Dunn, *Science* **2014**, *343*, 1210; b) Z. Cai, J. Wang, Y. Sun, *eScience* **2023**, *3*, 100093; c) C. Cai, X. Li, P. Hu, T. Zhu, J. Li, H. Fan, R. Yu, T. Zhang, S. Lee, L. Zhou, L. Mai, *Adv. Funct. Mater.* **2023**, *33*, 2215155; d) C. Li, R. Li, K. Liu, R. Si, Z. Zhang, Y. Hu, *Interdiscip. Mater.* **2022**, *1*, 396; e) Z. Wang, M. Zhou, L. Qin, M. Chen, Z. Chen, S. Guo, L. Wang, G. Fang, S. Liang, *eScience* **2022**, *2*, 209.

[3] a) M. Wu, W. Zheng, X. Hu, F. Zhan, Q. He, H. Wang, Q. Zhang, L. Chen, *Small* **2022**, *18*, e2205101; b) C. Luo, R. Qiu, G. Li, X. Shi, Z. Mao, R. Wang, J. Jin, B. He, Y. Gong, H. Wang, *Mater. Today Energy* **2022**, *30*, 101148; c) Y. M. Jung, J. H. Choi, D. W. Kim, J. K. Kang, *Adv. Sci.* **2023**, *10*, e2301160.

[4] a) H. Wang, C. Zhu, D. Chao, Q. Yan, H. J. Fan, *Adv. Mater.* **2017**, *29*, 1702093; b) T. Zhang, Z. Mao, X. Shi, J. Jin, B. He, R. Wang, Y. Gong, H. Wang, *Energy Environ. Sci.* **2022**, *15*, 158.

[5] a) Y. Zhou, J. Xia, J. Di, Z. Sun, L. Zhao, L. Li, Y. Wu, L. Dong, X. Wang, Q. Li, *Adv. Energy Mater.* **2023**, *13*, 2203165; b) K. Qu, X. Lu, Z. Huang, J. Liu, *Mater. Today Energy* **2022**, *30*, 101188; c) R. Fei, H. Wang, Q. Wang, R. Qiu, S. Tang, R. Wang, B. He, Y. Gong, H. J. Fan, *Adv. Energy Mater.* **2020**, *10*, 2002741.

[6] a) H. Tang, J. Yao, Y. Zhu, *Adv. Energy Mater.* **2021**, *11*, 2003994; b) S. Li, Y. Liu, X. Zhao, Q. Shen, W. Zhao, Q. Tan, N. Zhang, P. Li, L. Jiao, X. Qu, *Adv. Mater.* **2021**, *33*, 2007480; c) Y. Liu, L. Wu, *Nano Energy* **2023**, *109*, 108290; d) Y. Wan, T. Yun, X. Wang, B. Yao, Z. Ye, X. Peng, *Mater. Today Energy* **2023**, *36*, 101359.

[7] a) J. Chen, L. Wang, M. Peng, T. Hu, K. Yuan, Y. Chen, *Chem. Mater.* **2023**, *35*, 4089; b) X. Li, J. Hu, M. Wu, C. Guo, L. Bai, J. Li, Y. Li, D. Luo, J. Duan, X. Li, Z. Li, *Carbon* **2023**, *205*, 226; c) Y. Wang, S. Sun, X. Wu, H. Liang, W. Zhang, *Nano-Micro Lett.* **2023**, *15*, 78.

[8] a) X. Gao, H. Wu, C. Su, C. Lu, Y. Dai, S. Zhao, X. Hu, F. Zhao, W. Zhang, I. P. Parkin, C. J. Carmalt, G. He, *Energy Environ. Sci.* **2023**, *16*, 1364; b) X. Gao, H. Deng, Y. Fang, Y. Li, X. Lu, *Chin. Chem. Lett.* **2023**, *34*, 107919; c) W. Jian, W. Zhang, X. Wei, B. Wu, W. Liang, Y. Wu, J. Yin, K. Lu, Y. Chen, H. N. Alshareef, X. Qiu, *Adv. Funct. Mater.* **2022**, *32*, 2209914; d) S. Chen, Q. Kuang, H. J. Fan, *Small* **2020**, *16*, 2002803.

[9] a) H. v. Helmholtz, *Ann. Phys.* **1853**, *165*, 353; b) H. Shao, Y. C. Wu, Z. Lin, P. L. Taberna, P. Simon, *Chem. Soc. Rev.* **2020**, *49*, 3005.

[10] a) J. Luo, L. Xu, H. Liu, Y. Wang, Q. Wang, Y. Shao, M. Wang, D. Yang, S. Li, L. Zhang, Z. Xia, T. Cheng, Y. Shao, *Adv. Funct. Mater.* **2022**, *32*, 2112151; b) M. Hartmann, T. Clark, R. Eldik, *J. Am. Chem. Soc.* **1997**, *119*, 7843; c) E. R. Nightingale Jr., *J. Phys. Chem.* **1959**, *63*, 1381.

[11] J. Chmiola, G. Yushin, Y. Gogotsi, C. Portet, P. Simon, P. L. Taberna, *Science* **2006**, *313*, 1760.

[12] X. Li, Z. Liu, C. Cai, Q. Yu, W. Jin, M. Xu, C. Yu, S. Li, L. Zhou, L. Mai, *ChemSusChem* **2021**, *14*, 1756.

[13] X. Zhu, Y. Xia, X. Zhang, A. A. Al-Khalaf, T. Zhao, J. Xu, L. Peng, W. N. Hozzein, W. Li, D. Zhao, *J. Mater. Chem. A* **2019**, *7*, 8975.

[14] Y. F. Wang, Y. Liang, Y. F. Wu, J. Yang, X. Zhang, D. Cai, X. Peng, M. Kurmoo, M. H. Zeng, *Angew. Chem., Int. Ed.* **2020**, *59*, 13232.

[15] X. Hu, G. Wang, J. Li, J. Huang, Y. Liu, G. Zhong, J. Yuan, H. Zhan, Z. Wen, *Energy Environ. Sci.* **2021**, *14*, 4564.

[16] A. Jorio, A. G. Souza Filho, *Annu. Rev. Mater. Res.* **2016**, *46*, 357.

[17] P. Zhang, L. Wang, S. Yang, J. A. Schott, X. Liu, S. M. Mahurin, C. Huang, Y. Zhang, P. F. Fulvio, M. F. Chisholm, S. Dai, *Nat. Commun.* **2017**, *8*, 15020.

[18] H. Ma, H. Chen, M. Wu, F. Chi, F. Liu, J. Bai, H. Cheng, C. Li, L. Qu, *Angew. Chem., Int. Ed.* **2020**, *59*, 14541.

[19] C. Xia, Y. Xia, P. Zhu, L. Fan, H. Wang, *Science* **2019**, *366*, 226.

[20] L. Wang, M. Peng, J. Chen, X. Tang, L. Li, T. Hu, K. Yuan, Y. Chen, *ACS Nano* **2022**, *16*, 2877.

[21] A. C. Ferrari, D. M. Basko, *Nat. Nanotechnol.* **2013**, *8*, 235.

[22] a) A. C. Forse, C. Merlet, P. K. Allan, E. K. Humphreys, J. M. Griffin, M. Aslan, M. Zeiger, V. Presser, Y. Gogotsi, C. P. Grey, *Chem. Mater.* **2015**, *27*, 6848; b) M. Inaba, H. Yoshida, Z. Ogumi, *J. Electrochem. Soc.* **1996**, *143*, 2572.

[23] L. Wang, M. Peng, J. Chen, T. Hu, K. Yuan, Y. Chen, *Adv. Mater.* **2022**, *34*, 2203744.

[24] A. Chafidz, W. Astuti, V. Augustia, D. T. Novira, N. Rofiah, *IOP Conf. Series: Earth Environ. Sci.* **2018**, *167*, 012013.

[25] H. Xu, W. He, Z. Li, J. Chi, J. Jiang, K. Huang, S. Li, G. Sun, H. Dou, X. Zhang, *Adv. Funct. Mater.* **2022**, *32*, 2111131.

[26] A. Soni, M. Yusuf, V. K. Mishra, M. Beg, *Mater. Today: Proc.* **2022**, *68*, 710.

[27] L. Dong, X. Ma, Y. Li, L. Zhao, W. Liu, J. Cheng, C. Xu, B. Li, Q.-H. Yang, F. Kang, *Energy Storage Mater.* **2018**, *13*, 96.

[28] Z. Song, L. Miao, L. Ruhlmann, Y. Lv, D. Zhu, L. Li, L. Gan, M. Liu, *Adv. Mater.* **2021**, *33*, 2104148.

[29] a) Z. Supiyeva, X. Pan, Q. Abbas, *Curr. Opin. Electrochem.* **2023**, *39*, 101249; b) C. Zhao, Y. Lin, Q. Lin, Q. Liu, Y. Liu, Z. Liu, A. Ying, *Energy Storage Mater.* **2023**, *58*, 332.

[30] a) J. Yin, W. Zhang, W. Wang, N. A. Alhebshi, N. Salah, H. N. Alshareef, *Adv. Energy Mater.* **2020**, *10*, 2001705; b) J. Zeng, L. Dong, L. Sun, W. Wang, Y. Zhou, L. Wei, X. Guo, *Nano-Micro Lett.* **2020**, *13*, 19; c) K. Shang, Y. Liu, P. Cai, K. Li, Z. Wen, *J. Mater. Chem. A* **2022**, *10*, 6489; d) Y. Cao, X. Tang, M. Liu, Y. Zhang, T. Yang, Z. Yang, Y. Yu, Y. Li, J. Di, Q. Li, *Chem. Eng. J.* **2022**, *431*, 133241; e) F. Wei, Y. Wei, J. Wang, M. Han, Y. Lv, *Chem. Eng. J.* **2022**, *450*, 137919; f) H. Peng, X. Wang, Z. Liu, H. Lei, S. Cui, X. Xie, Y. Hu, G. Ma, *ACS Appl. Mater. Interfaces* **2023**, *15*, 4071; g) X. Li, J. Hu, M. Wu, C. Guo, L. Bai, J. Li, Y. Li, D. Luo, J. Duan, X. Li, Z. Li, *Carbon* **2023**, *205*, 226; h) Z. Li, D. Chen, Y. An, C. Chen, L. Wu, Z. Chen, Y. Sun, X. Zhang, *Energy Storage Mater.* **2020**, *28*, 307; i) L. Huang, Y. Xiang, M. Luo, Q. Zhang, H. Zhu, K. Shi, S. Zhu, *Carbon* **2021**,*185*, 1; j) Y. Zheng, W. Zhao, D. Jia, Y. Liu, L. Cui, D. Wei, R. Zheng, J. Liu, *Chem. Eng. J.* **2020**, *387*, 124161.

[31] T. Brezesinski, J. Wang, S. H. Tolbert, B. Dunn, *Nat. Mater.* **2010**, *9*, 146.

[32] H. Zhang, Q. Liu, Y. Fang, C. Teng, X. Liu, P. Fang, Y. Tong, X. Lu, *Adv. Mater.* **2019**, *31*, 1904948.

[33] Y. Gogotsi, P. Simon, *Science* **2011**, *334*, 917.